Journal of Nondestructive Evaluation (2025) 44:108
https://doi.org/10.1007/s10921-025-01250-5

Exploring Image Quality Improvements in High-Speed Dual Threshold Photon-Counting Micro-CT

Till Dreier[1] · **Jenny Romell**[1] · **Carlo Amato**[2] · **Spyridon Gkoumas**[2]

Received: 16 April 2025 / Accepted: 27 July 2025 / Published online: 18 August 2025

Abstract
High-speed X-ray computed tomography (CT) of batteries in-line or at-line is a promising technique to obtain quality-relevant insights leading to an optimized production process and detection of defective batteries. By using a high-power micro-focus X-ray source and a photon-counting detector, CT scans can be obtained within seconds. Here we explore utilizing the simultaneous readout of multiple images at different energy-discriminating thresholds and recombining them to improve the quality of the reconstructed volumes to optimize different quality parameters relevant to battery inspection. Using a-priori knowledge, threshold optimization is performed. Evaluating the combined volumes shows that there is an ideal threshold, or combination of two thresholds, depending on what matric used to optimize contrast between specific feature of a specific sample. Further, the contrast of the jelly roll compared to the rest of the battery can also be improved by combining two different thresholds. The experiments highlight the importance of threshold optimization and the potential gain of combining two simultaneous acquisitions using different energy thresholds for fast CT scans with limited photon statistics.

Keywords Computed tomography · Battery inspection · Liquid metal jet · Photon-counting detectors · Dual threshold · In-line inspection · At-line inspection

1 Introduction

With an increasing demand for electric vehicles (EVs), battery production is rapidly growing worldwide, both in scale and technological complexity. To ensure the quality and efficiency of the manufacturing process, sampling of batteries in- or at-line should be performed. This can give continuous and immediate feedback on the production process, which both leads to increased yield and minimizes the risk of faulty or damaged batteries being installed in an EV [1]. Among the many features of the assembled battery to be inspected in vicinity to the production line, X-ray computed tomography (CT) has been shown to address several key parameters [1–3]. These include anode/cathode overhang, winding accuracy of the jelly roll, particle contamination, debris and burr, as well as over- or under-winding of the anode, meaning how well the anode and cathode layers align at the beginning and end of the roll. These defects can lead to short circuits and, if not detected, cause vehicle fires and costly recalls for car manufacturers.

There are a number of destructive techniques that can be used to assess the quality of the individual components of the battery [4] but disassembly is often not acceptable. X-ray computed tomography, on the other hand, can give complete 3D data of battery samples, without taking the sample apart or altering its performance in any way [5]. This non-destructive analysis enables (a) *in situ/in operando* testing of battery electrodes [6] as well as (b) inspection of batteries in production.

While such research concerning battery development is mainly carried out at large-scale synchrotron facilities, which offer a multitude of analysis modalities at short exposure times, bringing the same high-speed performance for R&D to a local lab or factory has long been a challenge [7]. Developments in electron-impact x-ray sources, specifically the introduction of the MetalJet technology [8, 9], has increased the brightness available in a laboratory system manyfold and thus greatly decreased the exposure times

✉ Till Dreier
till.dreier@excillum.com

[1] Excillum AB, Stockholm, Sweden

[2] DECTRIS Ltd., Baden-Dättwil, Switzerland

needed for a CT scan [10]. Combined with fast efficient photon counting detectors [11], CT scanning on the second scale is becoming feasible.

If performed fast enough, the CT scans can provide immediate feedback in battery production, minimizing the risk that faulty batteries leave the factory. In- and at-line inspection are thus very important but present several challenges. When the total exposure time needs to be limited to a few seconds, the data will always contain a certain level of noise. The very short acquisition times, in the order of a few milliseconds per projection image, also puts high requirements on the imaging equipment, especially the x-ray source and the detector. Currently, photon-counting detectors are the best candidates for this task, offering high framerate, high efficiency and high resolution in combination with low noise [12, 13]. Additionally, photon counting detectors enable techniques such as material decomposition [14] and material-specific contrast improvement [15]. We have previously shown that a photon-counting detector used together with a high brightness MetalJet E1+X-ray source can enable overhang inspection in prismatic EV batteries imaged during a total scan time of 1 s [10], which is compatible with in-line inspection.

Despite using a powerful X-ray source and a highly efficient detector, at very short exposure times the number of photons reaching the detector is limited. Due to inherent randomness in X-ray generation, the emitted photons follow a Poisson distribution, which manifests as noise when detected [16]. For a polychromatic incident spectrum, a photon counting detector may also detect an incoming photon in more than a single pixel. This effect is called charge sharing– the detector effectively counts a photon more than a single time as long as the shared energy deposited in the adjacent pixels is still above the energy threshold [17]. When using lower energy thresholds, this a marginal reduction of the modulation transfer function, while when using higher energy thresholds, photons that spread their charge over more than a single pixel may not be counted at all due to the individual detected charges being below the energy threshold.

The current paper aims to explore another important feature of the photon-counting detectors, namely the simultaneous readout of images at multiple energy thresholds. We investigate whether a dual-threshold readout can increase the image quality of a battery scan, without increasing the scan time. Specifically, we image batteries of types 2170 (consumer cell) and 4680 (Li-ion EV cell) with the goal to optimize contrast between the anode and cathode layers by choosing and combining images acquired at different energy thresholds in the detector.

2 Methods

2.1 High-Speed Micro-CT of Batteries

All images were acquired with a high-speed micro-CT system at Excillum in Stockholm, Sweden (see Fig. 1). Using an Excillum MetalJet E1+X-ray source, which can provide up to 17 times higher flux than conventional solid-anode sources [18] while still operating with a small X-ray spot, scan times were kept in the few-seconds range for a full

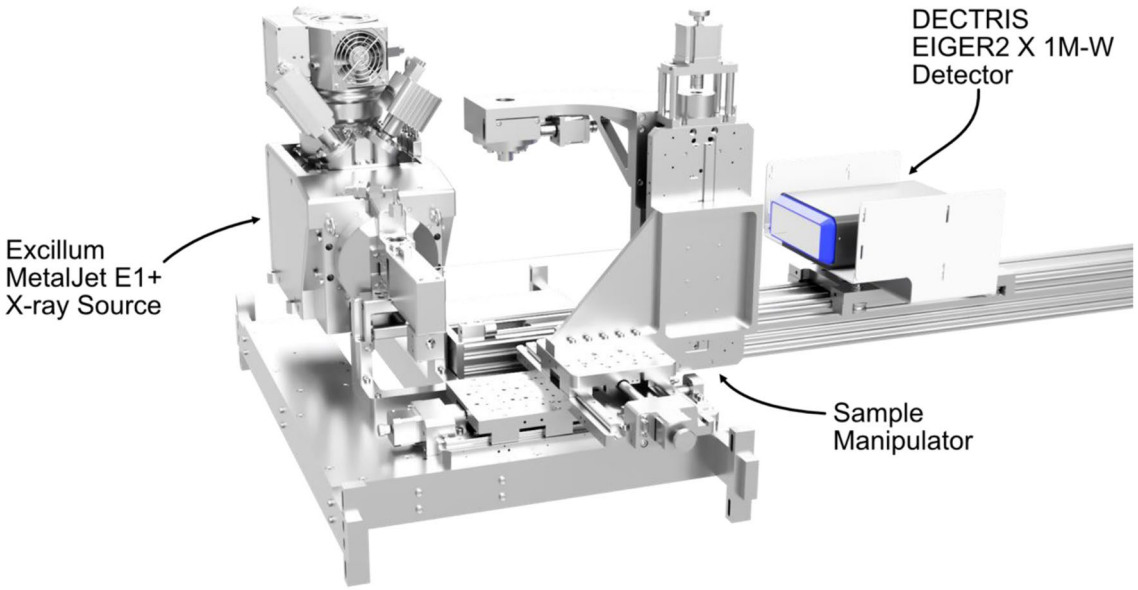

Fig. 1 A high-speed micro-CT system, based on the Excillum MetalJet E1+x-ray source, a DECTRIS EIGER2 X1 M-W photon-counting detector, an air-bearing rotation stage and linear stages enabling sample manipulation along three axes

Table 1 Imaging settings for two different batteries: 2170 and 4680

	2170	4680
Source-object distance	90 mm	150 mm
Source-detector distance	468 mm	468 mm
Magnification	5.2	3.1
Pixel size, object plane	14.4 µm	24 µm
Voxel size, reconstruction	20 µm	30 µm
Rotation speed	90 deg/s	90 deg/s
Exposure time	4 ms	20 ms
Readout time	continuous readout with 100 ns dead time	continuous readout with 100 ns dead time
Projections	1000	1000
Total scan time	4 s	20 s
Thresholds	15 & 20 keV, 33 & 36 keV, 50 & 55 keV	15 & 20 keV, 33 & 55 keV, 36 & 50 keV

CT. The X-ray source was operated at 160 kV and 700 W emission power with a 20 µm e-beam focus, which gives an effective X-ray spot of 30 µm. No filtration was added.

The battery samples, a 2170 consumer cell and a 4680 Li-Ion electric vehicle (EV) cell, were placed on a RT100S air-bearing rotation stage (LAB Motion Systems, Belgium) to enable tomographic imaging, with a maximum rotation speed of 3 Hz. Linear stages (Optics Focus, China) enabled sample manipulation along three different axes. The 2170 cell was positioned at a source-object distance (SOD) of 90 mm and the 4680 cell was placed at SOD = 150 mm.

A photon-counting detector, DECTRIS EIGER2 X CdTe 1M-W, with 75 µm pixel size, a 750 µm thick Cadmium Telluride (CdTe) sensor and an active area of 155.1 mm x 38.4 mm [11] was placed at a source-detector distance (SDD) of 468 mm, giving geometric magnification M = 5.2 for the 2170 cell and M = 3.1. A feature of this detector is the ability to acquire images at 2 different thresholds at the same time without affecting the image quality. The imaging settings for the two different batteries are summarized in Table 1.

In total, 3 scans were performed. Each scan was performed with 2 different thresholds with the goal to– after finding ideal settings for a specific use-case– to be able to acquire a scan with 2 optimal thresholds and combine the resulting volume into a single higher quality volume. The rotation stage was triggered to assure the volumes would align after reconstruction and all scans were acquired without removing the battery from setup. The battery was only moved up to acquire flat-field images for each threshold before the corresponding CT scan.

Several corrections were applied to the raw projection images. Dead pixels were removed, before the images were flat-field corrected using open-beam reference images. Preprocessing included interpolation of defective pixels and detector module gaps. For the 4680 cells, a multi-step ring removal was performed according to [19], implemented in Fiji [20]).

Reconstructions were performed using CERA (Siemens Healthineers, Germany) using the FDK cone-beam variant of filtered back-projection [21]. Finally, the reconstructed volume was virtually sectioned to better visualize and measure the signal of the anode/cathode layers and background. The reconstructed volumes are publicly available at [22].

2.2 Source and Detector Optimization

The detector allows for simultaneous readout of two images acquired at different energy thresholds up to a maximum frame rate of 1125 fps for two 16-bit images (2250 Hz for single threshold 16-bit images). Which threshold combinations to choose for the comparison was decided by analyzing the X-ray source spectrum (Fig. 2) as well as the attenuation in different materials of which the battery is

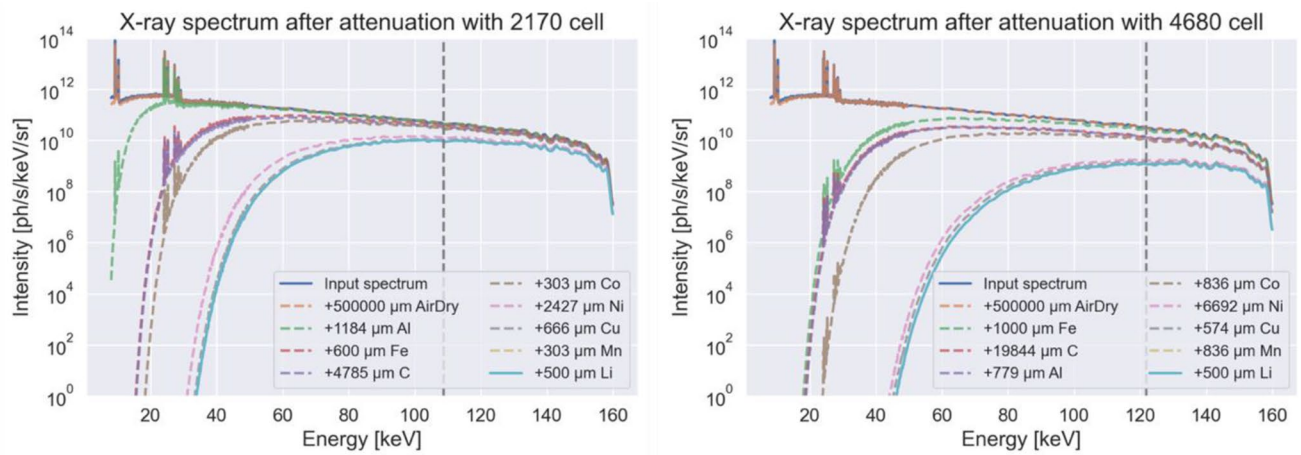

Fig. 2 X-ray spectra after attenuation with a 2170 cell (left) and a 4680 cell (right). The average energy of the spectrum is indicated by the gray vertical dashed line

composed and the quantum efficiency of the detector. The X-ray source spectrum was simulated using the Monte Carlo software PENELOPE (top blue lines in Fig. 2) and the attenuation of the different battery components (Li-Ion with NMC811–80% Ni, 10% Mn, 10% Co) was calculated to get an estimate of the X-ray spectrum behind the battery (bottom blue line in Fig. 2). The battery attenuation model was built based on [23] and [24].

The contrast between anode (consisting of a 10 µm copper foil with graphite coating, 50 µm on each side) and cathode (a 10 µm aluminium foil with 50 µm coating of NMC811, on each side) should be maximized. The attenuation of these materials was therefore simulated at relevant X-ray energies as shown in Fig. 3. Ideally, to maximize contrast, the difference in attenuation should be as large as possible. The optimal energy range for high attenuation difference would be between 15 and 75 keV. However, as shown by the attenuation simulation (Fig. 2), almost no photons < 40 keV are expected to penetrate the sample. On the other hand, higher energy photons > 100 keV will not contribute to contrast significantly.

Using the known detector response to different energy photons [11] allows to optimize the detector settings to obtain maximum performance. Based on the source and detector characteristics, six different energy thresholds were chosen: Two low-energy thresholds (15 and 20 keV), two medium-energy thresholds (33 and 36 keV) and two high-energy thresholds (50 and 55 keV). The goal with the low-energy thresholds was to maximize statistics and contrast at the trade-off a larger than single-pixel point-spread-function and increased scattering contribution to the signal. As shown in Fig. 2, the 2170 cell is expected to practically absorb all photons below 30 keV and the 4680 cell will absorb almost all photons below 40 keV. Hence, a large number of photons detected in the lower energy bins will be scattered photons or caused by charge sharing. The medium-energy thresholds were chosen above the Cd and Te fluorescence, to ensure improved PSF and spectral threshold separation, and at energies where the detector has approx. 70–80% efficiency (see [11]) and the contrast between the battery components is expected to be good (as indicated in Fig. 3). Finally, for the high-energy thresholds, around half the average energy of the attenuated spectrum was chosen (see Fig. 2), where a significant part of the emitted spectrum will penetrate the sample. The attenuation differences (shown in Fig. 3) are somewhat smaller, but the detector efficiency is still at approx. 70% at 50 keV and decreasing to ca. 40% at 100 keV.

To determine which of the two energy thresholds should be used, and how to combine them, three different methods were used:

1. Histogram CNR optimization.
2. Area CNR optimization.
3. Anode/cathode contrast optimization.

All three methods are described in detail below. Method one is performed on the single threshold images, while methods 2 and 3 utilize weighted averages (from 0 to 100% in steps of 10%) of all combinations of 2 thresholds.

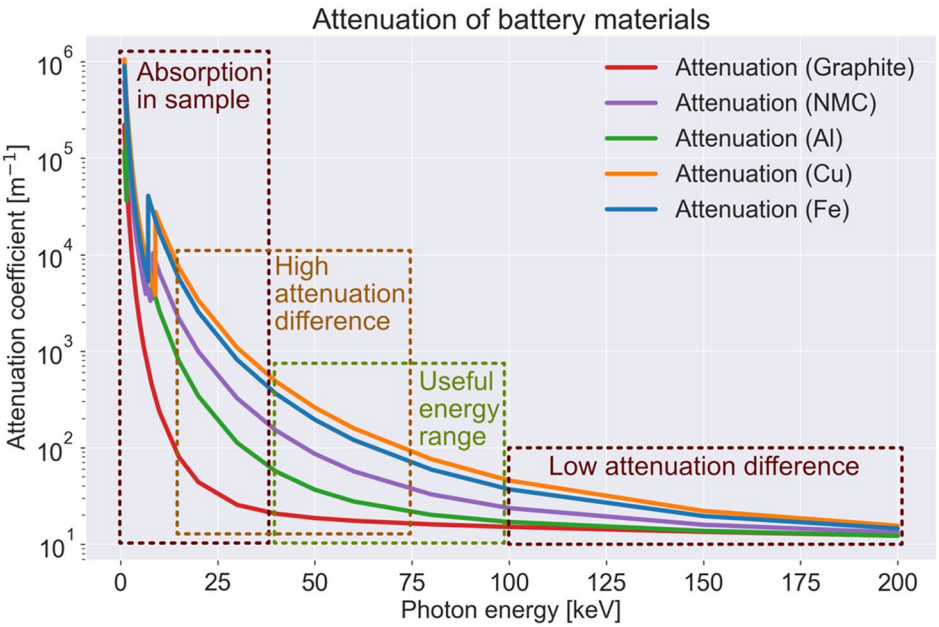

Fig. 3 Attenuation coefficients of the materials in a battery for energies between 0 and 200 keV, showing a region with high absorption in the sample (0–40 keV), a region with high attenuation difference (15–75 keV), a region with low attenuation difference (100–200 keV), and the main energy range useful for imaging (40–100 keV)

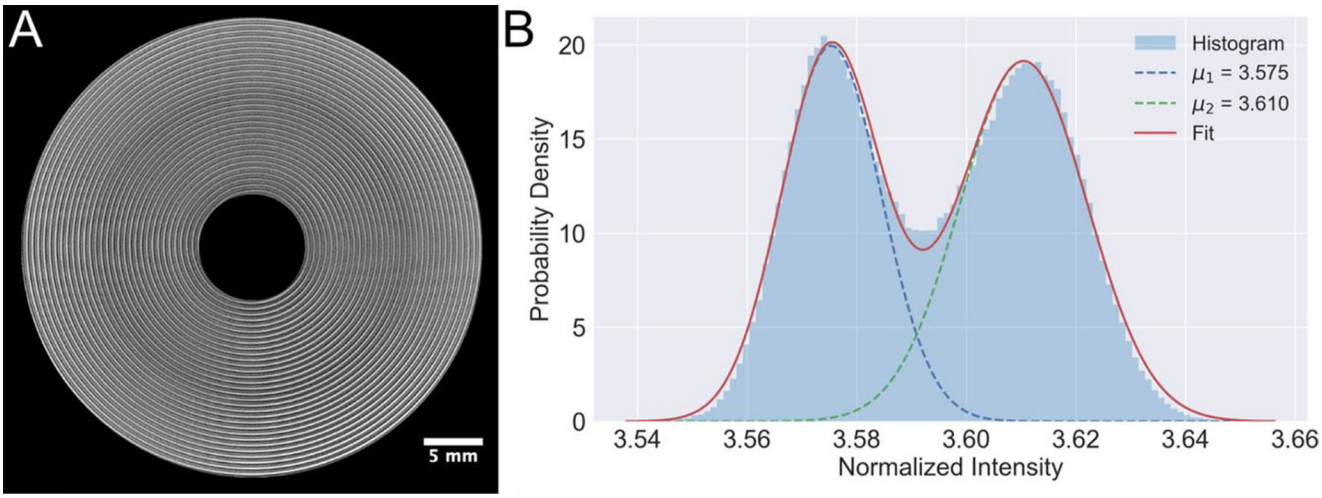

Fig. 4 **A**: Example of the annular ROI placed in the battery for histogram evaluation, where shell and core have been excluded. **B**: Example of the grey value histogram in the annular ROI. The histogram has been fitted with the sum of two gaussians to extract the mean attenuation of the high- and low- absorbing materials

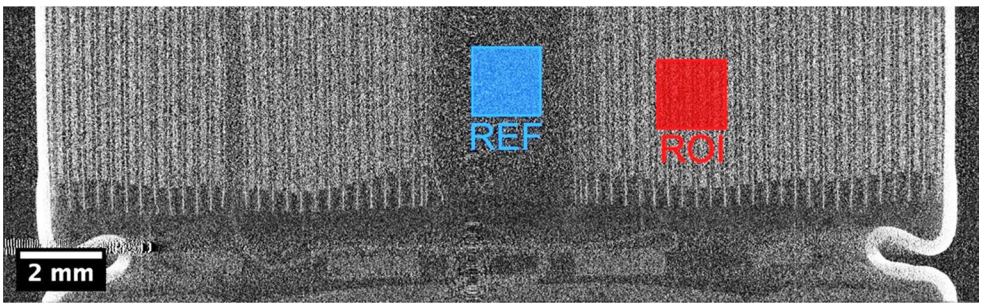

Fig. 5 Position of the regions chosen for CNR calculations: Region-of-interest (ROI) and reference (REF). The regions are 128 by 128 pixels

2.3 Image Quality Optimization

2.3.1 Histogram CNR Optimization

The first optimization method aims to characterize how the contrast-to-noise ratio (CNR) between the different features in the jelly roll changes as a function of the energy threshold. To select regions to compare, the histogram of gray values was used to assess the mean and standard deviation of the more attenuating (Cu and NMC) and less attenuating materials (Al and graphite). A thick annular ROI was drawn in the battery reconstruction so neither the battery housing nor core were included in the evaluation (Fig. 4A). The histogram of gray values in this ROI was fitted with a double gaussian to estimate the means (μ_i)and standard deviation (σ_i) for both material classes (Fig. 4B).

Then, the CNR was calculated as:

$$CNR_{\text{hist}} = \frac{|\mu_1 - \mu_2|}{\sqrt{\sigma_1^2 + \sigma_2^2}} \tag{1}$$

This CNR evaluation was repeated for both batteries and for all the energy thresholds.

2.3.2 Area CNR Optimization

Another optimization method is to improve the contrast of the jelly roll compared to the rest of the battery, e.g. to improve overhang measurements. The CNR is more reliable than signal-to-noise ratio (SNR) when analyzing low statistics very noisy data, as in the case of high-speed scans. Contrary to the histogram-based CNR analysis (Eq. (1)), here CNR is calculated using 2 ROIs containing either part of the sample or background, which is defined by

$$CNR_{\text{area}} = \frac{|s - n|}{\sigma_n} \tag{2}$$

where s is the mean of ROI, n is the mean of REF, and σ_n the standard deviation of REF. The ROI and REF regions are shown in Fig. 5. It should be noted that all reconstructed slices presented here are single slices, no averaging was applied.

2.3.3 Anode/cathode contrast Optimization

For inspection of the quality of the anode and cathode layers, the contrast between the layers should be maximized, improving detection of e.g. winding accuracy, delamination, or foreign particles. For each reconstructed dataset, a vertical virtual slice through the battery was selected to show the cross-section perpendicular to the anode and cathode layers. An example can be seen in Fig. 6. The image shows a single slice of 20 µm thickness from a 4 s CT scan of a 2170 battery cell. The image was acquired at a detector energy threshold of 15 keV. A line profile, 100 pixels wide, made from 130 averaged stacked lines (Fig. 6), was extracted, as shown by the red line, covering about 2 mm containing 6 cathodes and 5 anodes of the jelly roll. Cathodes appear as wider peaks with a dip in the middle, due to the aluminium collector, while the anodes appear as narrow peaks from the copper foil used as collector while the graphite coating is not visible. The peaks have been identified by applying a peak finding algorithm ("*find_peaks*" from the Scipy package) to data (blue), where the data has been maximum filtered.

Detector thresholds were combined two-by-two using weighted average and then the relative contrast between anode and cathode was calculated using Michelson contrast:

$$C = \frac{I_{\text{cathode}} - I_{\text{anode}}}{I_{\text{cathode}} + I_{\text{anode}}} \tag{3}$$

where C is the relative contrast and $I_{cathode}$ and I_{anode} are the normalized measured intensities at the peaks corresponding to cathode (wider peak with a dip in the middle) and anode (narrow peak), respectively.

The weighted average between combinations of thresholds were also compared to summed projections (15 keV, 20 keV) and summed (15 keV, 20 keV) reconstructed slices.

3 Results and Discussion

3.1 Histogram CNR Optimization

The contrast-to-noise (CNR) between the high- and low-attenuating materials of the jelly roll was calculated according to Eq. (1) by fitting the histogram of grey values with a double gaussian. For both battery types and all the investigated energy thresholds, the CNR normalized to the value at 15 keV is plotted in Fig. 7.

For both batteries, the CNR exhibits a dependency on the selected energy thresholds. The CNR for the 2170 battery has a peak at 36 keV which is 10% higher than the CNR measured at 15 keV. Further increases in the energy threshold led to a decrease of the CNR. For the 4680 battery, the CNR behavior is similar but more significant. The peak is broader and flat, and found for energies between 36 keV and 50 keV with a maximum value of 40%. This suggests that an actual absolute maximum higher than 40% might be observed for an energy threshold in between 36 keV and 50 keV. The possibility of further increasing the CNR for the features of interest, stresses the importance of a proper energy threshold selection when working with photon counting detectors.

The varying CNR behaviors between the two batteries are attributed to their distinct compositions and thicknesses. These two parameters affect not only the intensity, but also the hardness of the transmitted spectrum. It can be hypothesized that the CNR maximum for the 4680 battery is found at a higher energy compared to the 2170 because the thicker battery transmits a harder spectrum and absorbs approximatively all the photons below 50 keV (see Fig. 2). Therefore, all the signal detected below 50 keV is due to charge sharing, not by low-energy transmitted photons. According to the results, the CNR highly benefits by neglecting this contribution from the overall signal, and the high 50 keV

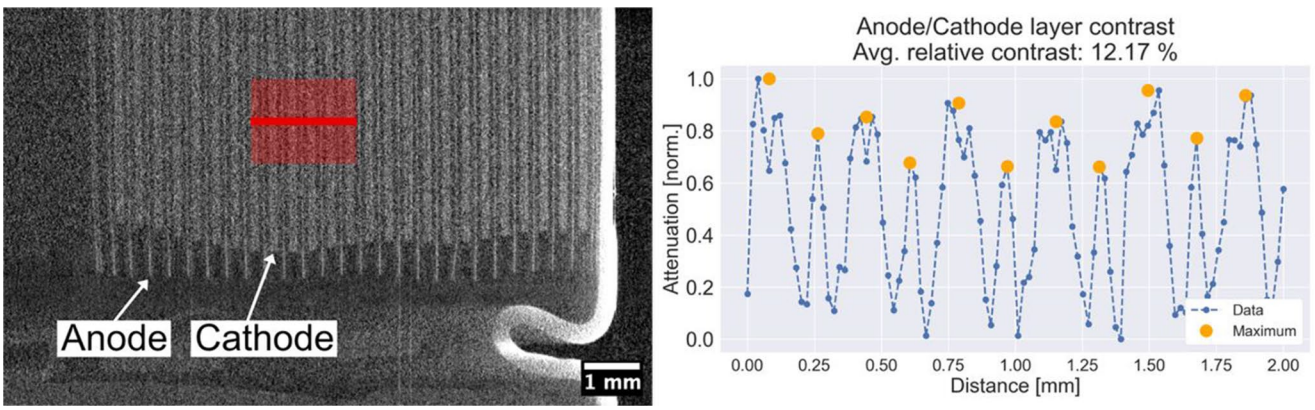

Fig. 6 Left: Example of a vertical virtual slice through a 2170 battery from a 4s CT scan. The narrow anodes can be distinguished from the wider cathode layers. The red line indicated the position of the line profile shown in the right figure. Right: Intensity profile across 2 mm of the jelly roll, including 6 cathode layers and 5 anodes. Measured data is shown in blue and the position of the maximum intensity of the anodes and cathodes is shown by orange dots

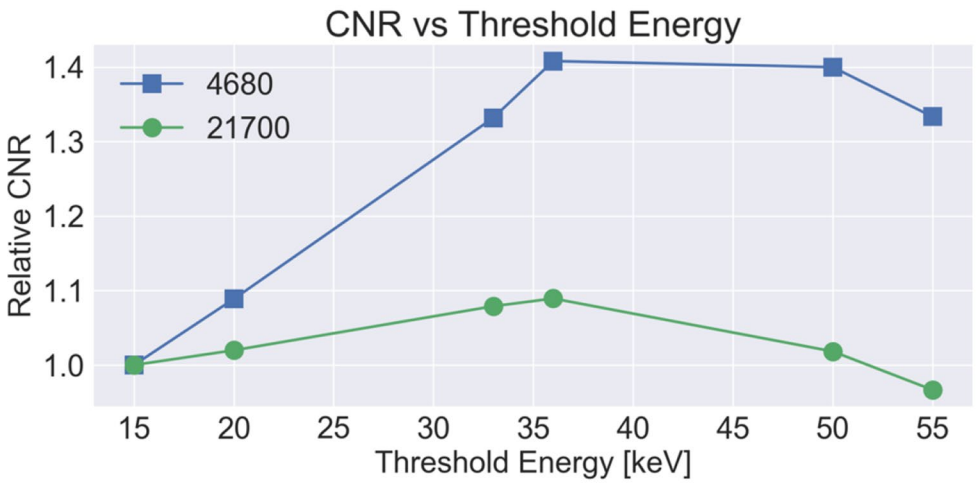

Fig. 7 Relative CNR between the battery components as distinguished by separation of histogram peaks, for all chosen energy thresholds. Data from the 2170 cell is shown in orange (lower curve) and from 4680 in blue

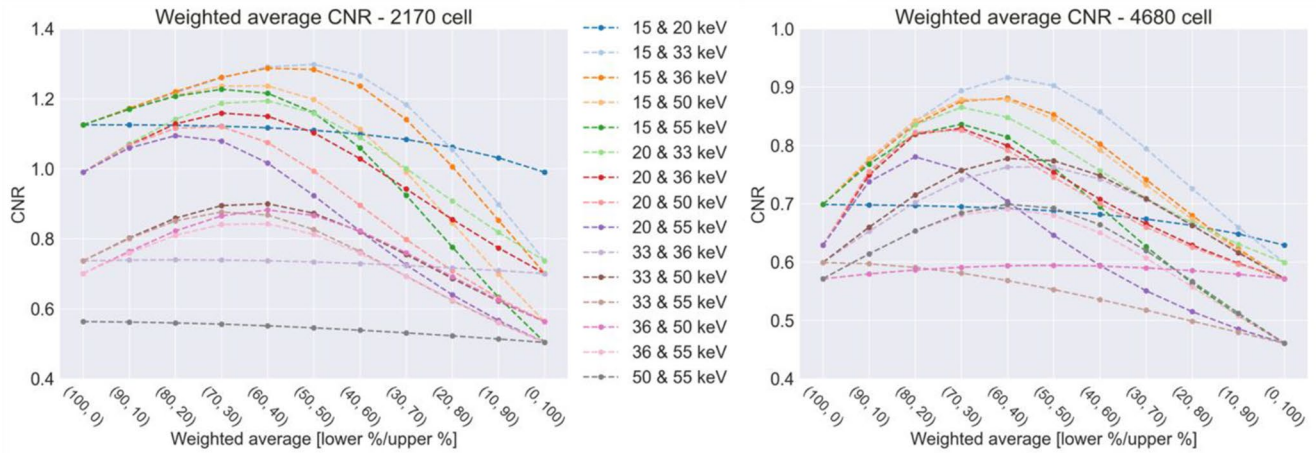

Fig. 8 Contrast-to-noise ratio for the 2170 (left) and the 4680 cell (right) for different weighted average combinations of the chosen energy thresholds. The CNR is typically maximized when combining data from two different thresholds. The exceptions seem to be combinations of two low, two medium or two high-threshold datasets

threshold may compensate as threshold equivalent beam hardening correction.

3.2 Area CNR Optimization

The CNR (Eq. (2)) was calculated for all possible combinations of low, medium and high energy detector thresholds optimizing the contrast between jelly roll and the rest of the battery. The CNR results are summarized in Fig. 8, for the 2170 cell (left) and the 4680 cell (right).

The combination of well separated thresholds, e.g. 15 and 36 keV or 33 and 50 keV, always seems to result in a maximum of the CNR curve at some ratio of the two parts with up to 50% improvement in CNR compared to using a single threshold image. Which ratio of the combination is most beneficial varies with the different thresholds. Combining 20 keV threshold data with a threshold at medium or high energy typically benefits from a larger contribution from the higher threshold. If the lower threshold is chosen to be 15 keV, or if the combination is a medium- and a high-energy threshold, a more even contribution is favorable for a high CNR. Combining close thresholds, such as 15 and 20 keV, 33 and 36 keV or 50 and 55 keV, provides no or no significant improvement to the CNR, possibly due to similar photon noise behavior at close energies.

An alternative, but more difficult, way of measuring the CNR could therefore be to calculate the CNR between the different layers in the jelly roll. The thinness of the layers, in combination with the high noise level, could however complicate such a measurement.

3.3 Anode/cathode contrast Optimization

The average relative contrast between anode and cathode for thresholds 33 and 55 keV (according to Eq. (3)), calculated for different weights from 0 to 100%, is shown in Fig. 9A for a 2170 battery. Figure 9B-D show examples of the image quality for some different weights as marked in

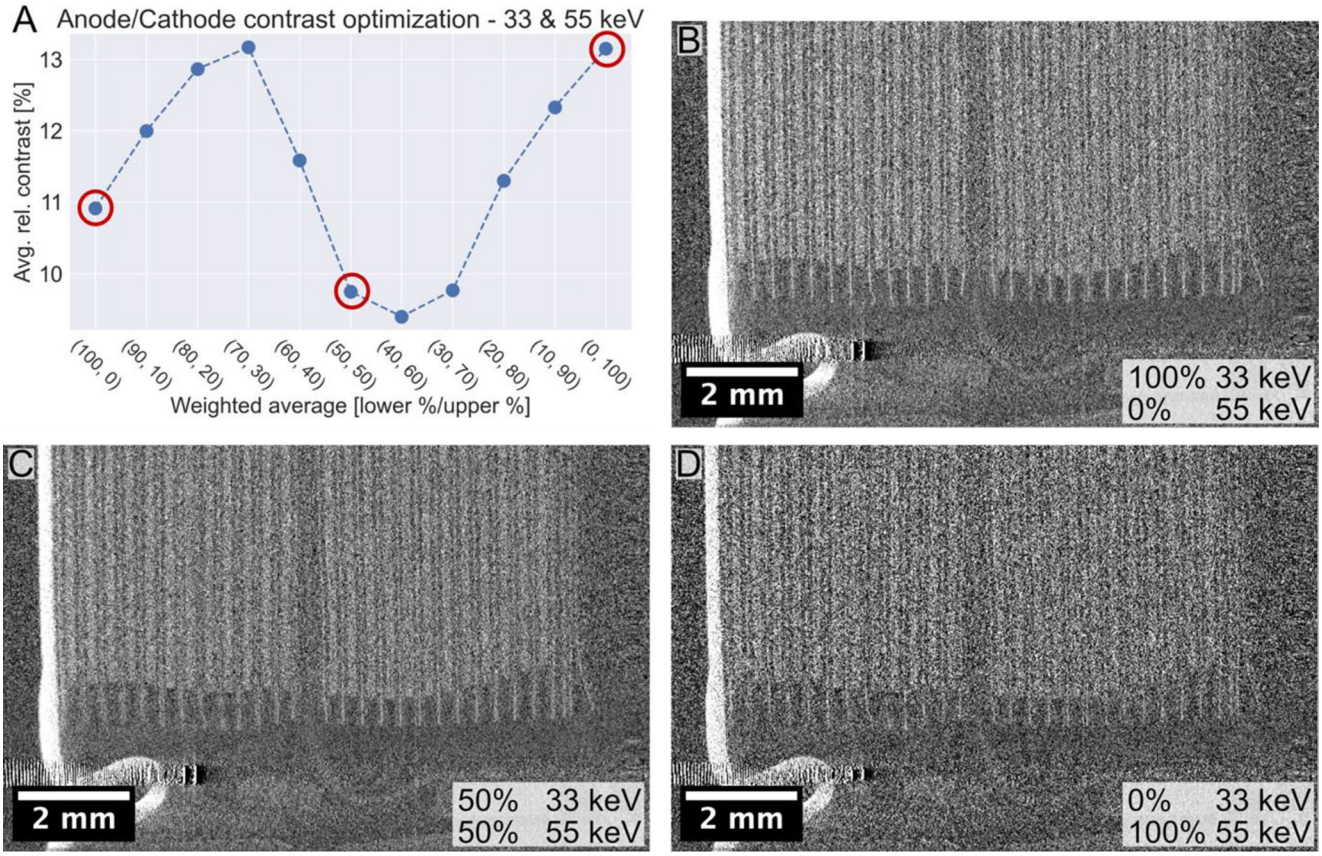

Fig. 9 Weighted average results composed of varying parts of the 33 and 55 keV threshold images of a 2170 battery. **(A)** Average relative contrast between anode and cathode for different weights of the two different thresholds. Examples of single slice CT data from datasets composed of **(B)** 100% 33 keV and 0% 55 keV, **(C)** 50% 33 keV and 50% 55 keV, and **(D)** 0% 33 keV and 100% 55 keV

Fig. 9A: 100% lower threshold (B), 50% lower/50% upper (C) and 100% upper threshold (D). All anode/cathode contrast curves are summarized in Fig. 11 for the 2170 cell and Fig. 12 for the 4680 cell.

Figure 11 shows the average relative contrast for all threshold combinations for a single virtual slice of 20 µm through a 2170 cell. In Fig. 12, the same data obtained from the 4680 cell is presented. The leftmost figures show the contrast from a combination of the 15 keV threshold images together with 20, 33, 36, 50 and 55 keV threshold data. Data containing the 20 keV threshold is presented in the middle figures, and the remaining data (combinations between medium and high thresholds) is shown in the rightmost figures.

For the 2170 cell (Fig. 11), the highest anode/cathode contrast was measured at a 70/30 ratio of 33 and 36 keV, closely followed by the case of 100% 36 keV data. The contrast was at a minimum when combining 36 and 55 keV data at a 40/60 ratio. Also using only a 20 keV threshold resulted in low contrast. The contrast curves for the 4680 cell (Fig. 12) show quite different trends, but the overall result is similar: Contrast is maximized when reconstructing with 100% 36 keV data. Lowest contrast for the 4680 cell is achieved with a 70/30 combination of 20 and 36 keV or a 60/40 combination of 20 and 50 keV. This highlights the benefits of threshold optimization when dealing with noise limited data. There may not be a benefit combining two noise-limited datasets.

A key limitation of comparing the relative contrast between anode and cathode layers in high-speed photon noise limited scans is the reliance on averaging to obtain a usable signal. Additionally, the data is normalized, hence, even small errors, artefacts, or changes can cause comparably large differences, as shown in Fig. 11 by e.g. combinations containing the 36 keV dataset. Reconstruction artefacts, defective pixels, or slight alignment offsets may have caused these relatively large changes highlighting the limited robustness of this method for noisy data.

Worth noting is that the CNR maximum (see Fig. 8) does not appear to correlate with the calculated maximum anode/cathode contrast (Figs. 11 and 12). This means that optimizing the threshold selection solely for CNR may give a lower contrast between the anode and cathode and hence not lead to any improvement in layer separation. Lastly, summing

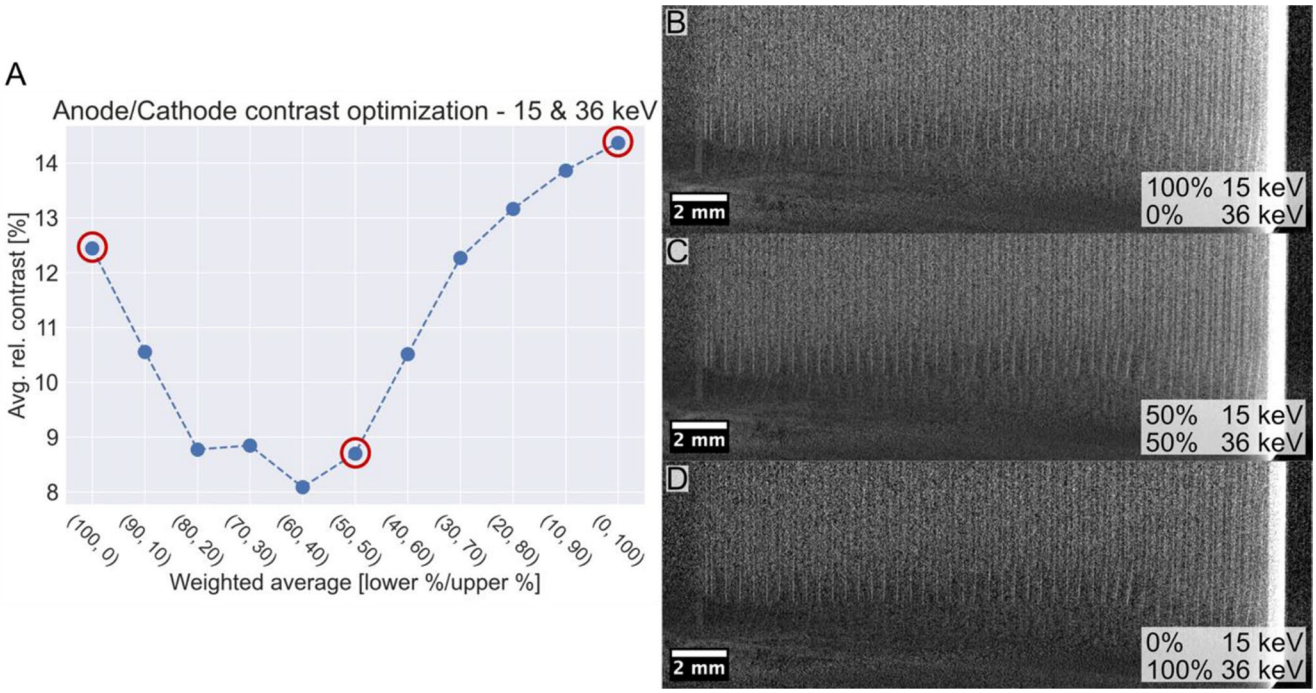

Fig. 10 Weighted average results composed of varying parts of the 15 and 36 keV thresholds for a 4680 battery cell. **(A)** Average relative contrast between anode and cathode across different ratios of the two thresholds. **(B)**, **(C)** and **(D)** show virtual vertical slices through the cell composed of 100% of the 15 keV data, 50/50 of 15 and 36 keV data, and 100% 36 keV data, respectively. Note the reduction in beam hardening with a larger portion of the higher-energy threshold, most evident from the glowing effect of the battery housing

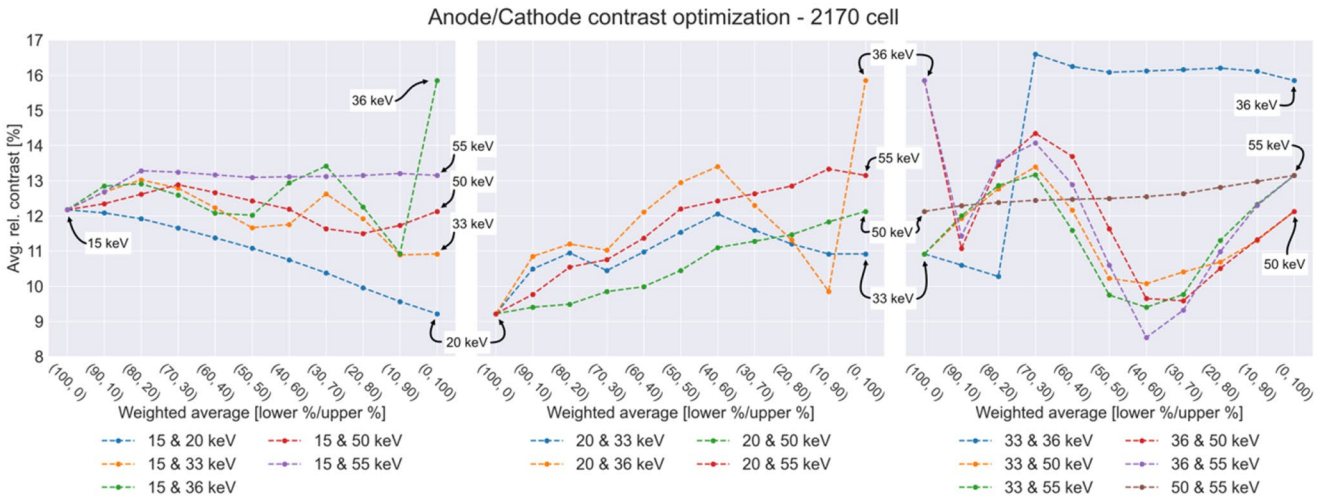

Fig. 11 Average relative contrast between anode and cathode for a 2170 cell, for all different combinations of the chosen low, medium and high energy thresholds

two close thresholds (15 keV, 20 keV) before or after reconstruction has always proven to be worse than using either of the thresholds or any weighted average of the two.

4 Conclusion

We have investigated the effect of different energy thresholds on image quality when using a photon-counting detector for the purpose of high-speed CT of batteries. In the case of high-speed scans and thus very short exposures, the data presents poor statistics and optimizing image quality becomes increasingly important to distinguish battery

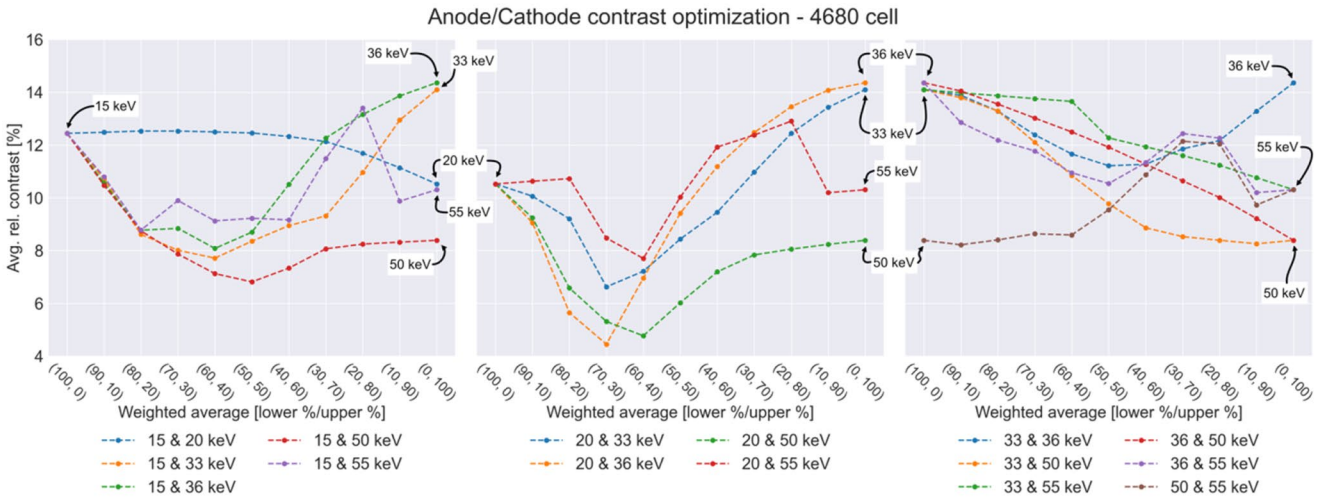

Fig. 12 Average relative contrast between anode and cathode for a 4680 cell, for all different combinations of the chosen low, medium and high energy thresholds

defects from noise. Three different methods of evaluating the image quality to select detector energy threshold were chosen: CNR based on the peaks in the histogram corresponding to anode and cathode, CNR calculated between jelly roll and the bulk of the battery, and anode/cathode contrast optimization. The different methods optimize the image contrast for different parameters and are hence of varying effectiveness for the overall image quality. For measuring winding accuracy, detecting particles or screening for damages in the anode and cathode layers, the histogram-based CNR calculation or anode/cathode contrast optimization should be used, while the area CNR, calculated between jelly roll and a reference area in the core of the battery, is better if optimizing for overhang measurements.

Among the six energy thresholds studied in this work, the histogram-based CNR calculation showed a clear indication to use a single 36 keV threshold, for both the battery types studied. For the 2170 battery, the increase in CNR is about 10% for the 36 keV threshold compared to 15 keV, while the same setting shows at least a 40% improvement for the 4680 cell. An interesting observation is the flatness of the CNR curve for the 4680 between the 36 and 50 keV thresholds, indicating that the actual peak is somewhere in between. This suggests that the optimal threshold has a dependence on battery type. Imaging of the larger, and more attenuating, 4680 cell may benefit from thresholding at a higher energy. Generally, this investigation has shown that threshold optimization has a significant impact on the contrast in the reconstructed volumes when working with noise-limited data.

When comparing contrast between anode and cathode, the conclusion is partly similar as to the histogram-based CNR. Weighted average calculations showed that dual-threshold reconstructions give no benefit in contrast compared to using a single threshold. For the batteries in this study (2170 consumer cell and 4680 lithium-ion EV cell), no combination has outperformed a single 36 keV threshold. On contrary to the histogram-based CNR calculation, the anode/cathode contrast for the 4680 battery was clearly the lowest when using a single threshold of 50 keV. Worth noting for both methods is the lack of data from the energies in between the chosen thresholds, where there is a possibility of contrast maxima at either a single energy threshold or some dual-threshold combination.

The area CNR calculation, which is useful for example for assessing anode/cathode overhang, shows significant benefits from combining data from two different energy thresholds, if the thresholds are well separated, the CNR can be improved by up to 50%.

In conclusion, this work highlights that optimization of the energy threshold is important for achieving the best possible image quality in high-speed CT using photon-counting detectors. Imaging arrangement, scan settings, and battery type including its geometry, chemistry and what defects are to be detected all need to be considered when choosing threshold. Future work includes investigation of further energy thresholds as well as expanding the calculations to include a larger variety of battery types, if possible, with known defects for a qualitative assessment of defect detectability.

Author Contributions T.D. and S.G. conceived the study, T.D. performed the measurements, T.D., J.R. and C.A. performed the data analysis, T.D. and C.A. prepared figures, J.R. wrote the manuscript with input from all authors, all authors reviewed the manuscript.

Data Availability The reconstructed volumes are available at osf.io/8635y, raw data can be made available upon request.

Declarations

Competing Interests T.D. and J.R. are employees of Excillum AB. S.G. and C.A. are employees of DECTRIS Ltd.

References

1. Atkins, D., Capria, E., Edström, K., Famprikis, T., Grimaud, A., Jacquet, Q., Johnson, M., Matic, A., Norby, P., Reichert, H., Rueff, J.-P., Villevieille, C., Wagemaker, M., Lyonnard, S.: Accelerating battery characterization using neutron and synchrotron techniques: Toward a Multi-Modal and Multi-Scale standardized experimental workflow. Adv. Energy Mater. **12**, 2102694 (2022)
2. Schromm, T., Beckmann, F., Moosmann, J., Berthe, D., Pfeiffer, F., Grosse, C.: Challenges in nondestructive Xray CT testing of riveted joints in the automotive industry, Discover Applied Sciences, vol. 6, 333 (2024)
3. Hemberg, O., Otendal, M., Hertz, H.M.: Liquid-metal-jet anode electron-impact x-ray source. Appl. Phys. Lett. **83**, 1483–1485 (2003)
4. Excillum, A.B.: The metal-jet technology, [Online]. Available: https://www.excillum.com/products/metaljet/. [Accessed 10 April 2025]
5. Dreier, T., Nilsson, D., Espes, E.: In-line and at-line battery CT enabled by MetalJet sources, in 13th Conference on Industrial Computed Tomography, Wels, Austria, (2024)
6. Donath, T., Jung, D.S., Burian, M., Radicci, V., Zambon, P., Fitch, A.N., Dejoie, C., Zhang, B., Ruat, M., Hanfland, M., Kewish, C.M., van Riessen, G.A., Naumenko, D.: Amenitsch and bourenkov, EIGER2 hybrid-photon-counting X-ray detectors for advanced synchrotron diffraction experiments. J. Synchrotron Radiat. **30**(4), 723–738 (2023)
7. Martinez-Garcia, J., Gwerder, D., Schiffmann, D., Thuering, T., Jung, D., Gkoumas, S., Schuetz, P.: Energy-selective X-ray CT imaging with an EIGER2 hybrid photon counting detector in a Diondo d2 XCT system, in 13th Conference on Industrial Computed Tomography, Wels, Austria, (2024)
8. Ballabriga, R., Alozy, J., Bandi, F.N., Campbell, M., Egidos, N., Fernandez-Tenllado, J.M., Heijne, E.H.M., Kremastiotis, I., Llopart, X., Madsen, B.J., Pennicard, D., Sriskaran, V., Tlustos, L.: Photon counting detectors for X-Ray imaging with emphasis on CT, ieee transactions on radiation and plasma medical scienceS, **5**, 4, p. 422, (2021)
9. Solem, R., Dreier, T., Gonçalves, I., Bech, M.: Material decomposition in Low-Energy Micro-CT using a Dual-Threshold photon counting X-Ray detector. Front. Phys. **9**, 673843 (2021)
10. Amato, C., Klein, L., Wehrse, E., Rotkopf, L.T., Sawall, S., Maier, J., Ziener, C.H., Schlemmer, H.-P., Kachelrieß, M.: Potential of contrast agents based on high-Z elements for contrast-enhanced photon-counting computed tomography, medical physics, **47**(12), 6179-6190 (2020)
11. Huda, W., Abrahams, R.B.: Radiographic techniques, contrast, and noise in X-Ray imaging. Am. J. Roentgenol. **204**(2), 126–131 (2015)
12. Zambon, P., Radicci, V., Trueb, P., Disch, C., Rissi, M., Sakhelashvili, T., Schneebeli, M., Broennimann, C.: Spectral response characterization of CdTe sensors of different pixel size with the IBEX ASIC. Nucl. Instrum. Methods Phys. Res., Sect. A. **892**, 106–113 (2018)
13. Excillum, A.B., MetalJet: E1+, [Online]. Available: https://www.excillum.com/products/metaljet/metaljet-e1/. [Accessed 10 April 2025]
14. An, K., Wang, J., Zhou, R., Liu, F., Wu, W.: Ring-artifacts removal for photon-counting CT. Opt. Express. **28**, 25180–25193 (2020)
15. Schindelin, J., Arganda-Carreras, I., Frise, E., Kaynig, V., Longair, M., Pietzsch, T., Preibisch, S., Rueden, C., Saalfeld, S., Schmid, B., Tinevez, J.-Y., White, D.J., Hartenstein, V., Eliceiri: Fiji: An open-source platform for biological-image Analysis. Nat. Methods. **9**, 676–682 (2012)
16. Feldkamp, L.A., Davis, L., Kress, J.: Practical Cone-beam algorithm. J. Opt. Soc. Am. **1**, 612–619 (1984)
17. Dreier, T., Romell, J., Amato, C., Gkoumas, S.: Open Science Framework, 15 April 2025. [Online]. Available: www.osf.io/8635y
18. Ank, M., Sommer, A., Gamra, K.A., Schöberl, J., Leeb, M., Schachtl, J., Streidel, N., Stock, S., Schreiber, M., Bilnger, P., Allgäuer, C., Rosner, P., Hagemeister, J., Rößle, M., Daub, R.: Lithium-Ion cells in automotive applications: Tesla 4680 cylindrical cell teardown and characterization. J. Electrochem. Soc. **170**, 120536 (2023)
19. Battery Design, 18 November: [Online]. (2022). Available: https://www.batterydesign.net/tesla-4680-cell/. [Accessed 14 April 2025]
20. Kim, J., Park, S., Hegazy, M., Lee, S.: Comparison of a photon-counting-detector and a CMOS flat-panel-detector for a micro-CT, in 2013 IEEE Nuclear Science Symposium and Medical Imaging Conference Seoul, Korea,(2013) NSS/MIC
21. L. A. Feldkamp, L. Davis and J. Kress, "Practical Cone-beam Algorithm," Journal of the Optical Society of America, vol. 1, pp. 612-619, 1984.
22. T. Dreier, J. Romell, C. Amato and S. Gkoumas, "Open Science Framework," 15 April 2025. [Online]. Available: www.osf.io/8635y.
23. M. Ank, A. Sommer, K. A. Gamra, J. Schöberl, M. Leeb, J. Schachtl, N. Streidel, S. Stock, M. Schreiber, P. Bilnger, C. Allgäuer, P. Rosner, J. Hagemeister, M. Rößle and R. Daub, "Lithium-Ion Cells in Automotive Applications: Tesla 4680 Cylindrical Cell Teardown and Characterization," Journal of The Electrochemical Society, vol. 170, p. 120536, 2023.
24. "Battery Design," 18 November 2022. [Online]. Available: https://www.batterydesign.net/tesla-4680-cell/. [Accessed 14 April 2025].
25. J. Kim, S. Park, M. Hegazy and S. Lee, "Comparison of a photon-counting-detector and a CMOS flat-panel-detector for a micro-CT," in 2013 IEEE Nuclear Science Symposium and Medical Imaging Conference (2013 NSS/MIC), Seoul, Korea, 2013.